Chapter 2

Fundamental Design Consideration of VCSELs

In this chapter, we initially illustrate various types of VCSEL devices. The fundamental design principles of VCSELs are then discussed, followed by a brief description of the threshold conditions and design of DBRs. The well-known rate equations are introduced to determine the steady state characteristics of VCSELs. Finally, the basic theory of DBRs as VCSEL resonator mirrors is discussed.

2.1 Typical Lateral Confinement Schemes of VCSELs

For assisting to understanding the characteristics of VCSELs, the brief introduction of device configuration is necessary. The longitudinal structure of a VCSEL device has been described in the use of DBRs and active quantum wells for current injection as well asother optical properties. Limiting the cross sectional areas of the electrical current and optical mode effectively in the vicinity of the gain region is important for achieving high efficiency or low threshold current. Hence, for all different structures of VCSELs, the main goal of process consideration is to provide a limited lateral extent and make the unwanted losses as low as possible. In Figure 2.1, we show the four device configurations used for transverse electrical or optical confinement. The basic properties of those different types of VCSELs are as follows.

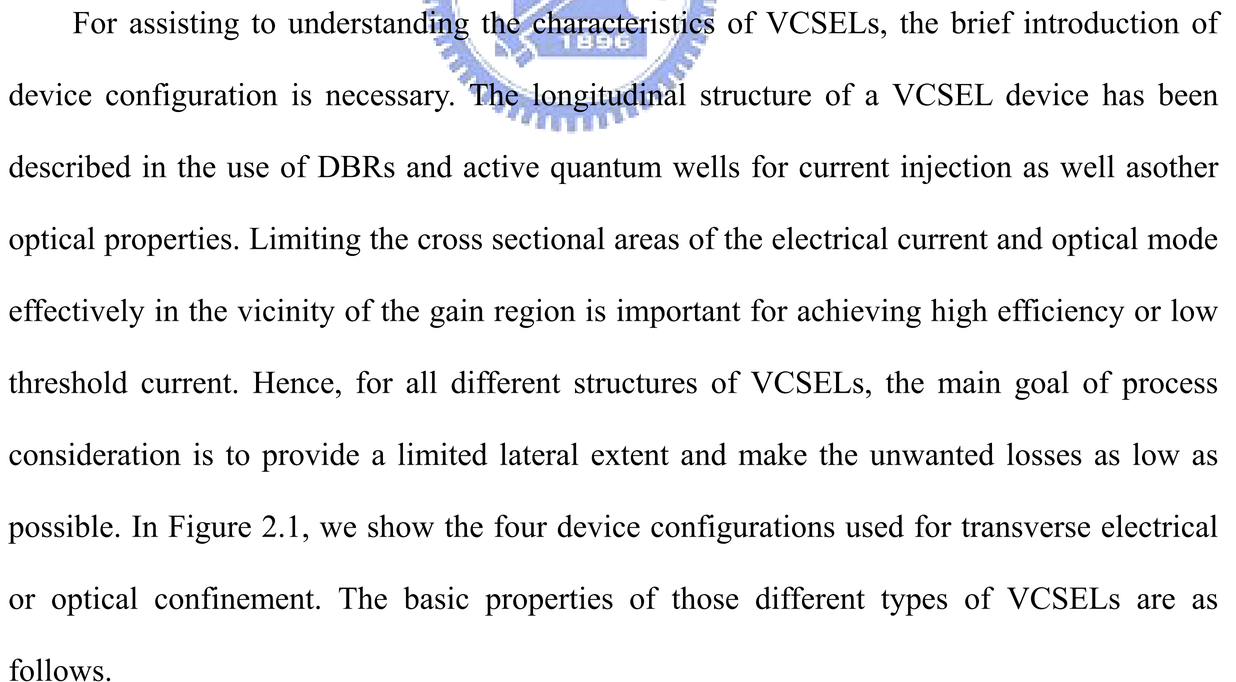

2.1.1 Air-Post Structures

To etch a pillar or post is the simplest technique to define the lateral dimensions of a VCSEL cavity【Figure 2.1(a)】. The circular or rectangular air-post with small diameter and smooth vertical sidewalls for lateral confinement is formed by anisotropic dry etching techniques, such as chemically assisted ion beam etching (CAIBE)【17】 or reactive ion etching (RIE)【18】. Strong index guiding is present in an air-post structure because of the large index step at the interface between semiconductor and air. As a result, the lateral dimension of the VCSEL resonator has to be relatively small (<5μm) if single transverse mode operation is desired【19】.

A disadvantage of the air-post VCSEL is carrier loss due to surface recombination at the side walls. In addition, optical loss increases with greater etch depth and smaller diameter, due to diffraction【20】 and scattering from imperfections in the sidewalls【21】, respectively. An additional consideration of air-post VCSELs is the thermal property relative to the roll over of output power. The heat sink material is removed from the laser cavity around, therefore, the reduced thermal dissipation leads to high thermal impedance which has a dramatic impact on laser performance.

2.1.2 Etched/Regrown Buried Heterostructures

To deposit other semiconductor materials after etching a pillar provides index guiding effect with a lower refractive index material selected around or another higher index material to form the anti-guiding condition for special uses【Figure 2.1(b)】. The provided materials can also be chosen with higher bandgaps as the effective current blocks. The problem that affects the air-post VCSELs for nonradiative recombination is released through the passivation on the sidewall of the active region. In addition, the regrown materials also provide good heat sinking that the device performance is much better than the air-post case in terms of larger operating current range and higher output power【22】.

The epitaxial regrowth is quite challenging for VCSELs because it typically requires growth on highly reactive AlGaAs surfaces. Three successfully demonstrated regrowth techniques to date include the dry etching with liquid phase epitaxy (LPE), the linked etching and molecular beam epitaxy (MBE) chambers with vacuum integrated, and the combination of dry and dry etching followed by chemical pretreatments before metal-organic vapor phase epitaxy (MOVPE)【23】. In spite of the improvements in performance compared to the air-post VCSELs, the complex fabrication techniques involving special cleaning, etching, and avoidance of exposure before regrowth are still considered expensive to the manufacturing area.

2.1.3 Ion-Implanted Structures

A planar VCSEL geometry provides better thermal dissipation as well as simplifies fabrication and packaging. To define the lateral current confinement in the planar structure, ion implantation has been widely used for the VCSEL fabrication【Figure 2.1(c)】. It uses ions such as H^+, O^+, N^+, and F^+ to implant into the specific region that becomes high electrical resistance or nonconductor, thus the injection current can not flow through this specific region. The required implantation energy depends on the ion mass and desired implant depth.

Implanted VCSELs have demonstrated good reliability【24,25】, in spite of the crystal damage caused by the implanted ions. However, the possibility of active region damage by ions and the indistinct boundary of the implanted region due to lateral scattering of ion species limit the proximity of the implanted region to the active layer and the precision with which small apertures can be defined. In addition, unlike the air-post structure, it does not provide inherent index guiding for the optical field. Hence, multilateral-mode operation is arising at higher injection level due to spatial hole burning (SHB).

2.1.4 Oxide-Confined Structures

Many recent advances in VCSEL performance are due to the use of selective oxidation to provide index guiding and electrical confinement【Figure 2.1(d)】. Wet oxidation of AlGaAs produces highly effective current apertures in hybrid VCSELs operating with dielectric DBRs【7】, as well as in monolithic VCSELs operating with semiconductor DBRs【26】.

The implementation of selective oxidation is relatively straightforward. One begins by growing Al rich AlGaAs layers at the desired locations of the current apertures. For lateral oxidation of the Al rich layers to occur, a mesa structure is formed by etching to expose the sidewalls. Placing the mesa structure in a stream environment at temperatures of 350 ℃ to 500 ℃ converts the AlGaAs to a robust insulating oxide with low refractive index【27】. The nonconductive and lower index of the oxide layer provides both electrical and optical confinements without damages in the mirror, caused by implantation and no surface recombination problems at the sidewall. The oxide-confined VCSELs with prior performance to other types of VCSELs soon arise with much attention to the VCSEL technology.

2.2 Threshold Condition

In the design of VCSELs with high internal quantum efficiency, threshold current density is one of the important parameters that must be optimized in the first place. In the following paragraphs, the equations of threshold current density for VCSELs are derived. In addition, the methods to minimize the threshold current density are discussed.

2.2.1 VCSELs with Bulk Active Layer

Figure 2.2 shows the schematic diagram of VCSELs with a uniform gain structure (UGS) used in the following analysis. An active layer is sandwiched between two longitudinal

confinement layers (p- and n-doped), forming a Fabry-Perot resonator. Mirrors on the surface of the confinement layers provide optical feedback for the standing wave, which is amplified inside the active region, along the longitudinal direction. In the diagram, it is assumed that the total cavity length of the VCSEL is L, the thickness of the active layer is d, the radius of the active region is W, and r_t, r_b (φ_t, φ_b) are the field reflectivity (phase) of the top and bottom mirrors, respectively.

The threshold conditions of VCSELs can be deduced using the approach of round-trip requirement. The optical field propagating along the longitudinal direction will be amplified inside the active region due to the stimulated emission but absorbed in the confinement layers. Part of the light will be reflected back into the laser cavity by the reflectors on the surface of the confinement layers, and the remaining optical field will emit to the surrounding area through the mirrors. Hence, the round-trip condition can be written as 【28,29】

$$1 = r_t r_b \exp[(g_{th} - \alpha_{diff})d - \alpha_{in} L] \cdot \exp[-j2k_0(n_{ac}d + n_{conf}(L-d)) - j(\varphi_t + \varphi_b)] \quad \textbf{(2.1)}$$

where $k_0 = 2\pi/\lambda_R$, λ_R is the lasing wavelength, α_{diff} represents the diffraction loss, α_{in} represents the total internal loss of the laser cavity, and n_{ac}, n_{conf} are the effective refractive index of the active and confinement layers, respectively. It can be shown from the real part of (2.1), the threshold gain, g_{th}, of the VCSELs is given by

$$\Gamma_z g_{th} = \alpha_{in} + \Gamma_z \alpha_{diff} + L^{-1}\ln(\frac{1}{R}) \quad \textbf{(2.2)}$$

where $R = r_t r_b$, $\Gamma_z = d/L$, is the longitudinal confinement factor which is defined as the portion of light confined within the active layer so that $\Gamma_z g_{th}$ can be explained as the effective threshold gain of VCSELs.

For an active region made of bulk materials, the corresponding threshold optical gain g_{th} at peak gain wavelength can be expressed in terms of injection carrier concentration at

threshold N_{th}, which is given by

$$g_{th} = g_N(N_{th} - N_t) \quad \textbf{(2.3)}$$

where g_N is the differential gain coefficient and N_t is carrier concentration at transparency. This is a linear approximation on the optical gain with the variation of injection carrier concentration. From the rate equation of carrier concentration, the threshold current density J_{th}, of the laser can be related to N_{th} as

$$J_{th}/qd = N_{th}/\tau_{eff} \quad \textbf{(2.4)}$$

where τ_{eff} is the effective carrier lifetime, and it can be approximated as a function of N_{th}

$$\frac{1}{\tau_{eff}} = \frac{1}{\tau_n} + B_{sp}N_{th} + C_{Aug}N_{th}^2 \approx B_{eff}N_{th} \quad \textbf{(2.5)}$$

where τ_n is the carrier lifetime, B_{sp} is the bimolecular radiative recombination coefficient, and C_{Aug} is the nonradiative Auger recombination coefficient. These coefficients represent the recombination of electrons and holes inside a semiconductor material, and the recombination process can be radiative or nonradiative. Then, substituting (2.2), (2.3) and (2.5) into (2.4), the expression of J_{th} can be written as

$$J_{th} = J_s d^2\left[\alpha_{in} + \Gamma_z\alpha_{diff} + L^{-1}\ln\left(\frac{1}{R}\right) + \Gamma_z g_N N_t\right]^2 \quad \textbf{(2.6)}$$

where $J_s = qB_{eff}/g_N^2\Gamma_z^2 d$, and the term $g_N N_t$ can be interpreted as the residual absorption loss of the optical gain.

2.2.2 VCSELs with Quantum-Well Active Layer

From (2.6), the threshold current density of VCSELs seems to be higher than that of edge emitting lasers due to the former's small cavity size. However, this threshold current density of VCSELs can be minimized if the value of g_N can be increased. In fact, enormous enhancement in g_N can be achieved by replacing the bulk active layer with QW material,

but the disadvantage is the reduction of the longitudinal confinement factor Γ_z with which the threshold current density is increased. Hence, using multiple quantum wells (MQWs) as the active layer can solve the problem of small Γ_z provided the high absorption loss inside the barriers and separate-confinement heterostructure (SCH) layers of MQWs can be avoided 【30】. If QW material is used as the active layer, it is more appropriate to replace the linear approximation on the optical gain and injection carrier concentration by the logarithmic gain-carrier density relation, as shown below【31,32】

$$g_{th} = a_N \ln\left(\frac{N_{th}}{N_t}\right) \quad \textbf{(2.7)}$$

where a_N is the gain coefficient. This equation represents the variation of optical gain at peak gain wavelength with injection carrier concentration. From (2.7), the differential gain at threshold can be written as $g_N = a_N/N_{th}$, where $g_N \sim 1\times10^{-15}\,\mathrm{cm}^2$ with $N_{th} \sim 2\times10^{18}\,\mathrm{cm}^{-3}$ is assumed in the calculation. Therefore, the magnitude of differential gain of QWs materials is about 10 times that of bulk materials.

Figure 2.3 shows the schematic bandgap energy of a MQW active layer used in the following analysis. If the length of VCSELs is much longer than the well width, the corresponding optical confinement of QWs Γ_w can be approximated by

$$\Gamma_w \approx \frac{n_w L_w}{L} \quad \textbf{(2.8)}$$

where n_w and L_w are the number and the thickness of the QWs, respectively. It is noted that the length of VCSELs with QW active regions is shorter than that with a bulk active region. The relation between threshold current density J_{th} and threshold carrier concentration of QWs N_{th} can be obtained from the rate equation of carrier concentrations inside the SCH (M) and QWs (N) layers as shown below【33】

$$\frac{\partial M}{\partial t} = \frac{J}{q n_w L_{SCH}} - \frac{M}{\tau_s} + \frac{L_w}{L_{SCH}}\frac{N}{\tau_{te}} \quad \textbf{(2.9 a)}$$

$$\frac{\partial N}{\partial t} = \frac{L_{SCH}}{L_w}\frac{M}{\tau_s} - \frac{N}{\tau_n} - \frac{N}{\tau_{te}} - v_g g(N) S$$

(2.9 b)

where L_{SCH} is the thickness of the SCH layers, τ_s is the ambipolar carrier transport time across the SCH layer, τ_n is the carrier lifetime in the QWs, τ_{te} is the thermionic emission lifetime from the quantum wells, g is the optical gain, and v_g is the group velocity. In the rate equations, the terms with τ_{te} represent the loss of carriers from the QW and the gain by the SCH layer. However, the terms with τ_s have opposite meanings. In addition, the finite capture time of the QW can be considered in the analysis through τ_s. Figure 2.3 shows the corresponding transport characteristic of M and N between the SCH and QW layers. Hence, with the assumption that the photon density is equal to zero (S=0) at threshold in (2.9), the expression of J_{th} can be deduced to be

$$\frac{J_{th}}{qn_w L_{SCH}} = \frac{1}{\tau_n}\frac{L_w}{L_{SCH}}N_{th} \quad \textbf{(2.10)}$$

where we assume that $N \rightarrow N_{th}$ and $J \rightarrow J_{th}$. If $\tau_n = (B_{eff}N_{th})^{-1}$ is assumed, the threshold current density J_{th} can be written as

$$J_{th} = J_s \exp\left\{\frac{2}{a_N \Gamma_w}\left[\alpha_{in} + \frac{1}{L}\left(\alpha_{diff} d + \ln\left(\frac{1}{R}\right)\right)\right]\right\} \quad \textbf{(2.11)}$$

where $J_s = qn_w L_w B_{eff} N_t^2$.

We use Eq.(2.11) to plot the calculated threshold current density J_{th} (threshold current I_{th}) of GaAs VCSELs against the diameter of active region, and number of QWs for the product of rear and back mirror reflectivity R, which varies between 0.985 and 0.998. Figure 2.4 shows the variation of threshold current density and threshold current with the diameter of active region. It is observed that the threshold current density decreases with the increase in the diameter of the active region and maintains uniform for 2W>1.5μm. The threshold current is defined as $I_{th} = J_{th} \cdot \pi \cdot W^2$. We can see that the threshold current

increases with the increase in the diameter of the active region in Figure 2.4. It is noted that when the diameter is less than 2μm, the diffraction losses is significant to the devices. Therefore, the threshold current increases with decreasing diameter. In addition, the higher mirror reflectivity achieves the lower threshold current (density). Figure 2.5 shows the variation of threshold current density with the number of QWs used as the active layer for different values of R. It is shown that the value of threshold current density reduces with the increase in n_w but remains unchanged for large values of n_w. It must be noted that the approximation of Γ_w by (2.8) may be invalid for large values of n_w, so the optimal values of n_w selected for both J_{th} and n_w are minimum values. The calculated parameters are summarized in Table 2.1.

2.3 Design and Analysis of Distributed Bragg Reflector

Opposite to their edge-emitting laser counterparts, VCSELs usually have thin active layers. To compensate that, VCSELs must have mirrors of much higher reflectivity than conventional edge-emitting lasers. High reflectivity can be obtained by coating an almost perfect conductor on the surface of the confinement layer. However, the high absorption from the metal coating is unavoidable; hence, dielectric or semiconductor multilayered mirrors with high reflectivity and low absorption loss are utilized in VCSELs.

Multilayered mirrors can be realized by using a series of dielectric or semiconductor layers in which the refractive index of each subsequent layer alternates in magnitude but with equal optical thickness of a quarter-wavelength. Therefore, the reflected waves interfere constructively at the design wavelength and produce a high reflection coefficient with a phase exactly equaling zero or π. Very high peak reflection coefficients can be obtained even if the number of dielectric layers is small【34】. Consisting of multiple layers with alternating high, low refractive indexes, the reflectivity of DBRs could easily exceed 99.9% and both reflectors

and active region could be monolithically grown.

2.3.1 Transfer Matrix Method

First consider the case of a single layer of dielectric of index n_1 and thickness d between two infinite media of indices n_0 and n_T. Figure 2.6 shows the wave vectors and their associated electric fields for the normal incidence on a single dielectric layer. The amplitude of the electric vector of the incident beam is E_0. That of the reflected beam is E_0', and that of the transmitted beam is E_T. The electric-field amplitudes in the film are E_1 and E_1' for the forward and backward traveling waves, respectively. The boundary conditions require that the electric and magnetic fields be continuous at each interface. The conditions are expressed as follows:

	First interface	*Second interface*
Electric	$E_0 + E_0' = E_1 + E_1'$	$E_1 e^{ikd} + E_1' e^{-ikd} = E_T$
Magnetic	$H_0 - H_0' = H_1 - H_1'$ or $n_0 E_0 - n_0 E_0' = n_1 E_1 - n_1 E_1'$	$H_1 e^{ikd} - H_1' e^{-ikd} = H_T$ or $n_1 E_1 e^{ikd} - n_1 E_1' e^{-ikd} = n_T E_T$

ES 1896

The phase factors e^{ikd} and e^{-ikd} result from the fact that the wave travels through a distance d from one interface to the other. If we eliminate the amplitudes E_1 and E_1', we obtain in matrix form

$$\begin{bmatrix} 1 \\ n_0 \end{bmatrix} + \begin{bmatrix} 1 \\ -n_0 \end{bmatrix} \frac{E_0'}{E_0} = \begin{bmatrix} \cos kd & \frac{-i}{n_1} \sin kd \\ -i n_1 \sin kd & \cos kd \end{bmatrix} \begin{bmatrix} 1 \\ n_T \end{bmatrix} \frac{E_T}{E_0} \quad \textbf{(2.12)}$$

which can be abbreviated as

$$\begin{bmatrix} 1 \\ n_0 \end{bmatrix} + \begin{bmatrix} 1 \\ -n_0 \end{bmatrix} r = M \begin{bmatrix} 1 \\ n_T \end{bmatrix} t \quad \textbf{(2.13)}$$

where $r = E_0'/E_0$ is the reflection coefficient and $t = E_T/E_0$ is the transmission coefficient. The matrix, known as the transfer matrix

$$M = \begin{bmatrix} \cos kd & \frac{-i}{n_1}\sin kd \\ -in_1 \sin kd & \cos kd \end{bmatrix} \quad \textbf{(2.14)}$$

Now suppose that we have N layers numbered 1, 2, 3, · · · N having indices of refraction $n_1, n_2, n_3, \cdots n_N$ and thicknesses $d_1, d_2, d_3, \cdots d_N$, respectively. In the same way that we derived Equation (2.13), we can obtain the reflection and transmission coefficients of the multilayer film are related by a similar matrix equation

$$\begin{bmatrix} 1 \\ n_0 \end{bmatrix} + \begin{bmatrix} 1 \\ -n_0 \end{bmatrix} r = M_1 M_2 M_3 \cdots M_N \begin{bmatrix} 1 \\ n_T \end{bmatrix} t = M \begin{bmatrix} 1 \\ n_T \end{bmatrix} t \quad \textbf{(2.15)}$$

The overall transfer matrix M is the product of the individual transfer matrices. Let the elements of M be A, B, C, and D, that is

$$M_1 M_2 M_3 \cdots M_N = M = \begin{bmatrix} A & B \\ C & D \end{bmatrix} \quad \textbf{(2.16)}$$

We can then solve Equation (2.15) for r and t in terms of these elements. The result is

$$r = \frac{An_0 + Bn_T n_0 - C - Dn_T}{An_0 + Bn_T n_0 + C + Dn_T}$$
$$t = \frac{2n_0}{An_0 + Bn_T n_0 + C + Dn_T} \quad \textbf{(2.17)}$$

The reflectance R and the transmittance T are given by $R = |r|^2$ and $T = |t|^2$, respectively.

2.3.2 Simulation Results of DBRs Reflectivity

Using the above equations, we can calculate the reflection spectrum of $Al_{0.12}Ga_{0.88}As/AlAs$ DBRs. The simulated VCSEL structure is shown in Table 2.2. In Figure 2.7(a), we show the calculated the reflection spectrum of top-DBR which is consisted of 20.5

$Al_{0.12}Ga_{0.88}As / AlAs$ pairs, and in Figure 2.7(b), we show the spectrum of bottom-DBR which is consisted of 30.5 $Al_{0.12}Ga_{0.88}As / AlAs$ pairs. The reflectance of top-DBR is 0.9985, and the reflectance of bottom-DBR is 0.9995. The number of pairs needed for the top DBR is fewer than the bottom due to the larger difference of index between air and top surface. As can be seen from the calculated results, the fewer the pair number is, the narrower the stop band of reflection spectrum.

A broader stop band can provide the better tolerance due to the shift of laser cavity mode, which can occur because of the increase in temperature under typical CW operation condition. The reflection spectrum of the completed VCSEL structure is shown in Figure 2.8. As can be seen from the spectrum, the cavity resonant dip is located at 845 nm. The calculated results are fitted in with our expectations of the real VCSEL structure.

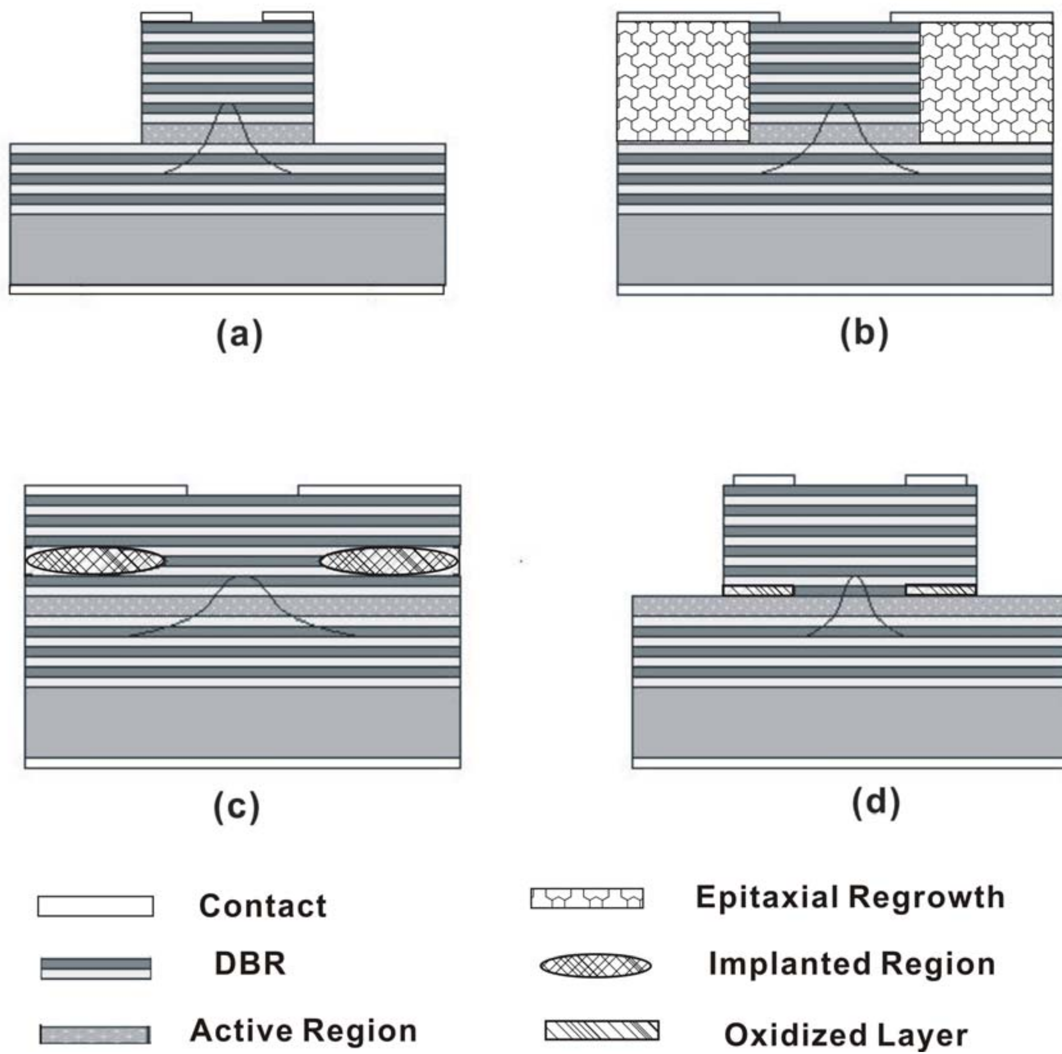

Figure 2.1 Structures of (a) air-post, (b) etched/regrown, (c) ion-implanted, (d) oxide-confined VCSELs.

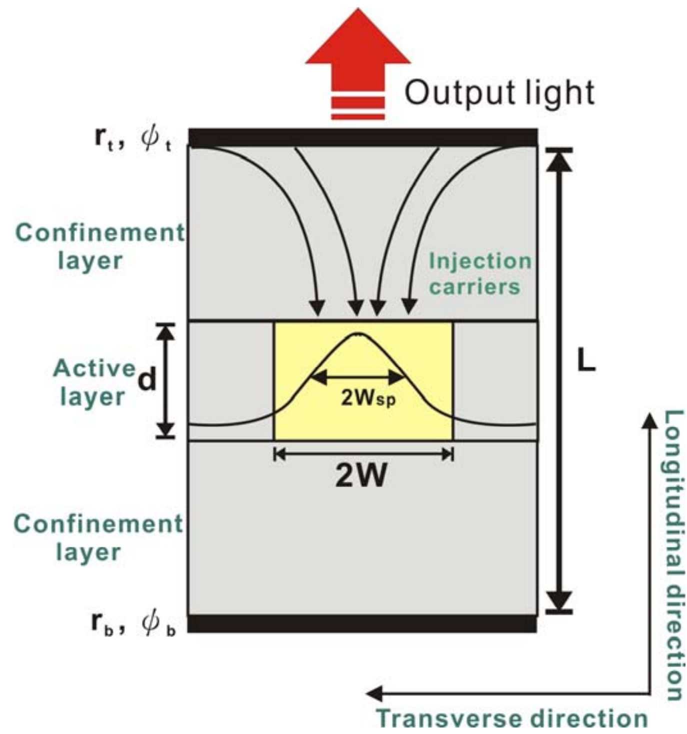

Figure 2.2 Schematic diagram of VCSELs with uniform gain structure.

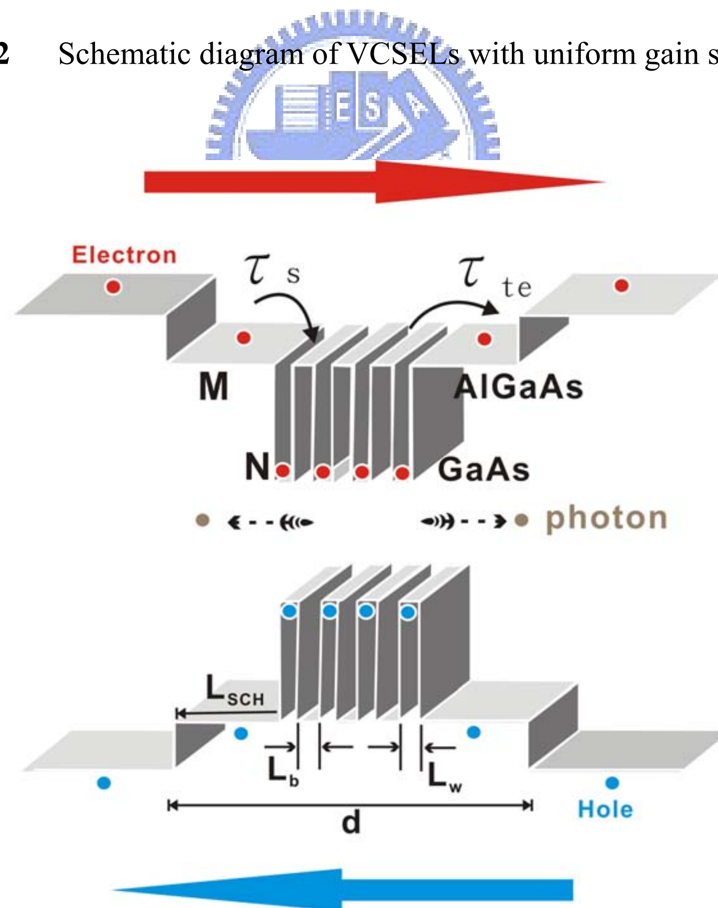

Figure 2.3 Scheme of a MQW with a separate confinement heterostructure.

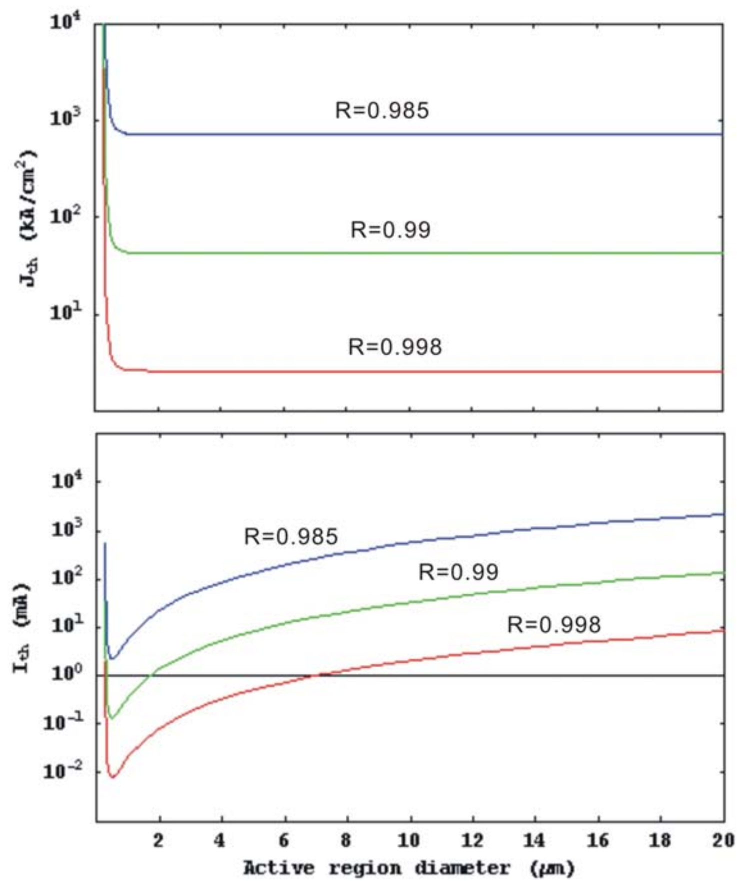

Figure 2.4 Threshold current density J_{th} and threshold current I_{th} against the diameter of active region 2W for VCSELs.

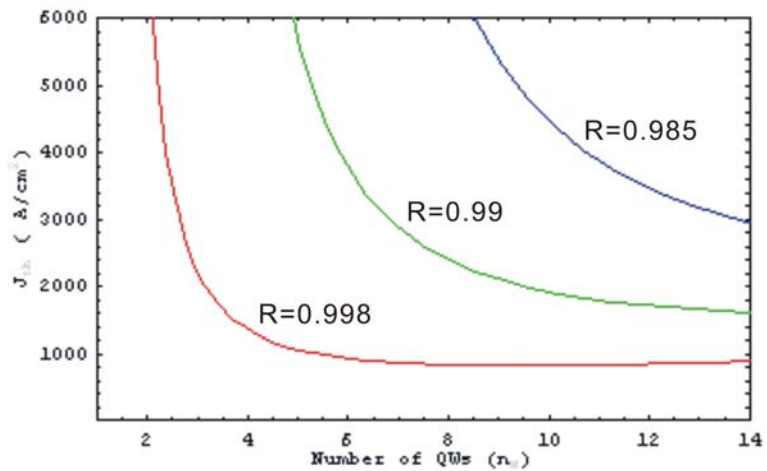

Figure 2.5 The dependence of threshold current density J_{th} on the number of quantum wells n_w with different values of reflectivity R.

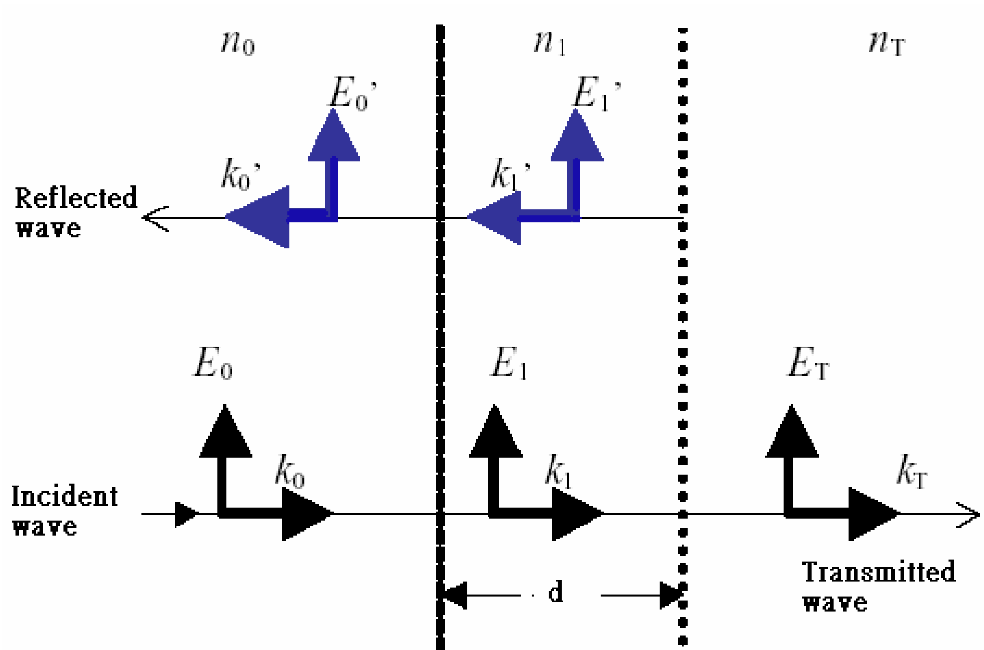

Figure 2.6 Wave vectors and their associated electric fields for the case of normal incidence on a single dielectric layer.

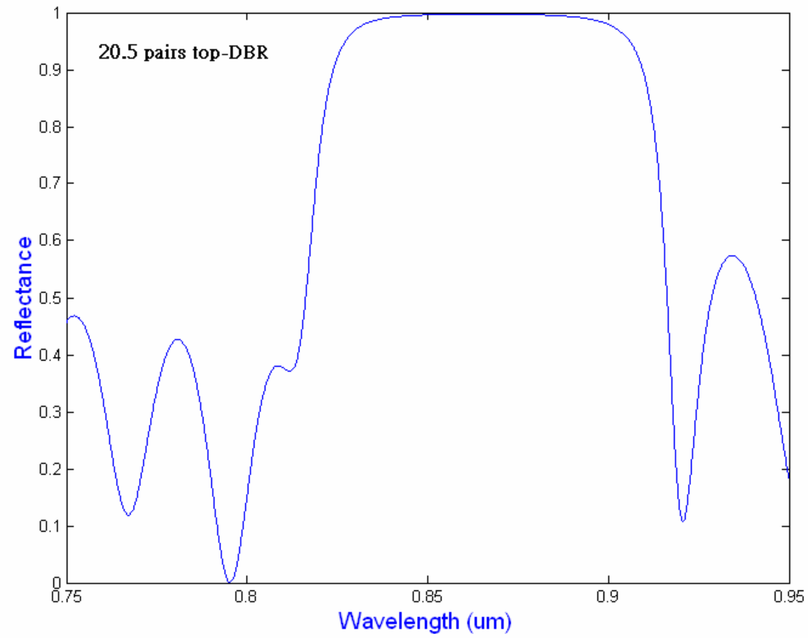

(a)

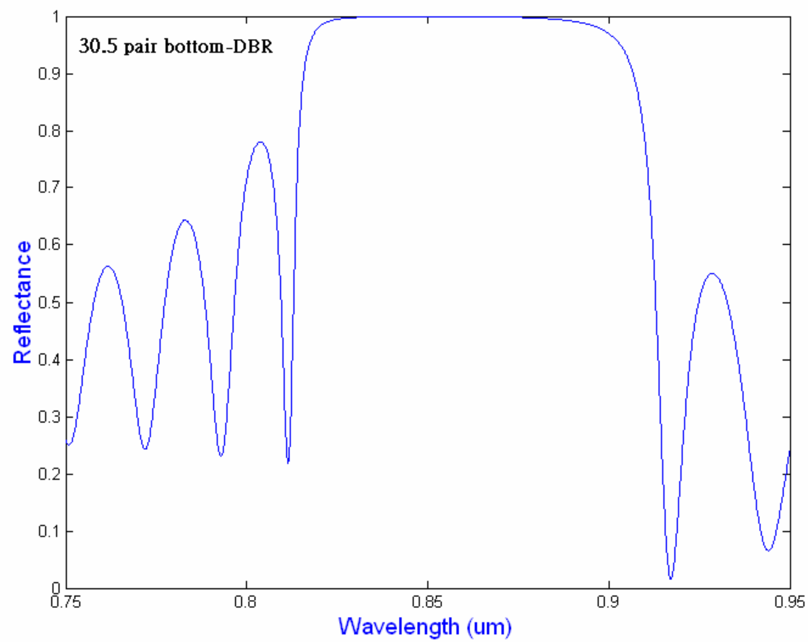

(b)

Figure 2.7 The reflection spectra of (a) top 20.5 pairs DBR, and (b) bottom 30.5 pairs DBR.

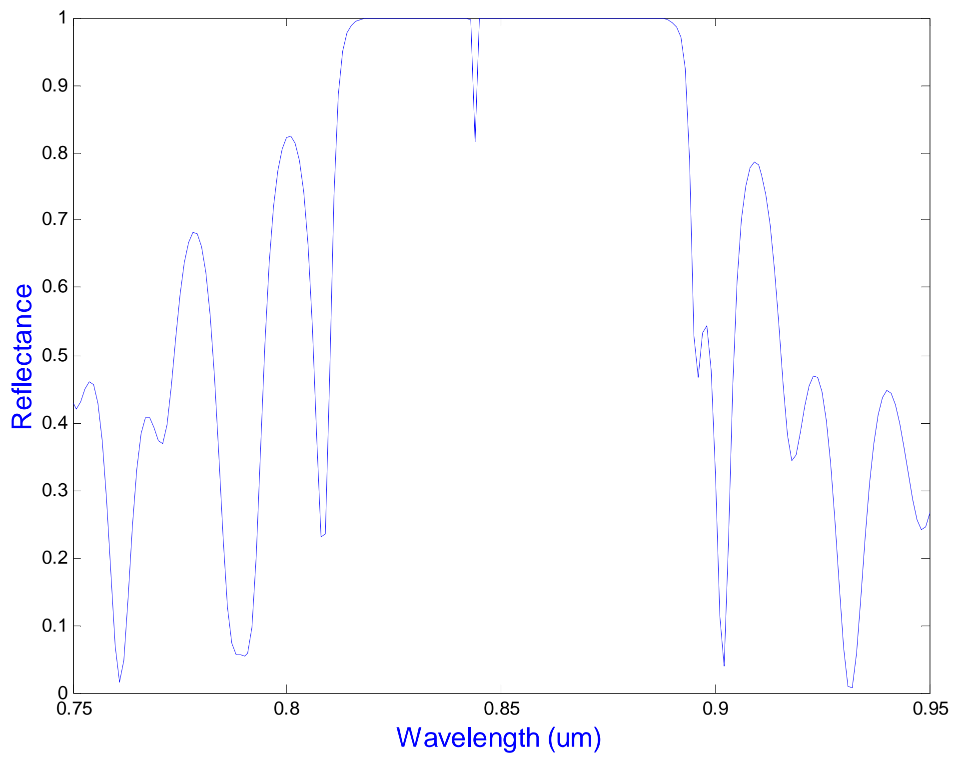

Figure 2.8 The reflection spectrum for 850 nm VCSEL with 20.5 pairs top-DBR and 30.5 pairs bottom-DBR.

Parameter(GaAs)	**Value (300K)**	Units
L	0.248	μm
d	0.074	μm
L_w	6	nm
L_b	8	nm
N_t	1.5×10^{18}	cm^{-3}
B_{eff}	1.5×10^{-10}	cm^3/s
a_N	2000	cm^{-1}
α_b	50	cm^{-1}
α_{SCH}	50	cm^{-1}
α_{ac}	50	cm^{-1}
α_{conf}	**10**	cm^{-1}

Table 2.1 Material parameters used in the calculation of the room temperature threshold current density of GaAs/AlGaAs VCSELs.

Layer	Material	Al Mole Fraction (X)	Thickness (μm)	Concentration (cm^{-3})	Type	Dopant
21	GaAs		**0.1150**	＞1E19	P	Zn/C
20	$Al_xGa_{1-x}As$	0.12	**0.2850**	＞1 E19	P	Zn/C
19	$Al_xGa_{1-x}As$	1.0 →	0.0100	3~5 E18	P	C
18 X	AlAs		0.0509	3~5 E18	P	C
17 X	$Al_xGa_{1-x}As$	0.12 →	0.0100	3~5 E18	P	C
16 X	$Al_xGa_{1-x}As$	0.12	0.0389	3~5 E18	P	C
15 X	$Al_xGa_{1-x}As$	1.0 →	0.0100	3~5 E18	P	C
14	AlAs		0.0609	3~5 E18	P	C
13	$Al_xGa_{1-x}As$	0.3 → 0.6	0.0870		U/D	
12	$Al_xGa_{1-x}As$	0.3	0.0100		U/D	
11 X	$Al_xGa_{1-x}As$	0.3	0.0080		U/D	
10 X	GaAs		0.0060		U/D	
9	$Al_xGa_{1-x}As$	0.3	0.0100		U/D	
8	$Al_xGa_{1-x}As$	0.6 → 0.3	0.0870		U/D	
7	AlAs		0.0609	1 ~ 3 E18	N	Si
6	$Al_xGa_{1-x}As$	0.12 →	0.0100	1 ~ 3 E18	N	Si
5 X	$Al_xGa_{1-x}As$	0.12	0.0389	1 ~ 3 E18	N	Si
4 X	$Al_xGa_{1-x}As$	1.0 →	0.0100	1 ~ 3 E18	N	Si
3 X	AlAs		0.0509	1 ~ 3 E18	N	Si
2 X	$Al_xGa_{1-x}As$	0.12 →	0.0100	1 ~ 3 E18	N	Si
1	GaAs		0.5	1 ~ 3 E18	N	Si

Table 2.2 The parameters of our ion-implanted VCSEL structure.